Spin and valence dependence of iron partitioning in Earth's deep mantle

Hélène Piet[a,1], James Badro[a,b], Farhang Nabiei[a,c], Teresa Dennenwaldt[c,d], Sang-Heon Shim[e], Marco Cantoni[c], Cécile Hébert[c,d], and Philippe Gillet[a]

[a]Earth and Planetary Science Laboratory, Institut de Physique, École Polytechnique Fédérale de Lausanne, CH-1015 Lausanne, Switzerland; [b]Institut de Physique du Globe de Paris, Sorbonne Paris Cité, CNRS, FR-75005 Paris, France; [c]Centre Interdisciplinaire de Microscopie Électronique, École Polytechnique Fédérale de Lausanne, CH-1015 Lausanne, Switzerland; [d]Laboratoire de Spectrométrie et Microscopie Électronique, Institut de Physique, École Polytechnique Fédérale de Lausanne, CH-1015 Lausanne, Switzerland; and [e]School of Earth and Space Exploration, Arizona State University, Tempe, AZ 85281

Edited by Barbara A. Romanowicz, University of California, Berkeley, CA, and approved August 8, 2016 (received for review April 1, 2016)

We performed laser-heated diamond anvil cell experiments combined with state-of-the-art electron microanalysis (focused ion beam and aberration-corrected transmission electron microscopy) to study the distribution and valence of iron in Earth's lower mantle as a function of depth and composition. Our data reconcile the apparently discrepant existing dataset, by clarifying the effects of spin (high/low) and valence (ferrous/ferric) states on iron partitioning in the deep mantle. In aluminum-bearing compositions relevant to Earth's mantle, iron concentration in silicates drops above 70 GPa before increasing up to 110 GPa with a minimum at 85 GPa; it then dramatically drops in the postperovskite stability field above 116 GPa. This compositional variation should strengthen the lowermost mantle between 1,800 km depth and 2,000 km depth, and weaken it between 2,000 km depth and the D″ layer. The succession of layers could dynamically decouple the mantle above 2,000 km from the lowermost mantle, and provide a rheological basis for the stabilization and nonentrainment of large low-shear-velocity provinces below that depth.

iron partitioning | lower mantle | spin state | valence state | viscosity

The relative concentration (partitioning) of iron in minerals constituting mantle rocks is a critical parameter controlling their physical properties and, consequently, the dynamical properties of the mantle. In a pyrolitic mantle, the lower-mantle mineral phase assemblage consists of bridgmanite (Brg)—which transforms to postperovskite (PPv) at pressures higher than 110 GPa (1–4)—ferropericlase (Fp), and calcium silicate perovskite. Only Brg/PPv (hereafter referred to as "silicate" and abbreviated Sil) and Fp can accommodate significant amounts of iron in their structure (5). Density, elasticity, viscosity, and thermal or electrical conductivities, along with associated phase relations, melting temperatures, and relative melt/solid buoyancy, are all linked to the concentration, valence, and spin state of iron in lower-mantle minerals. The seismic observation of global-scale heterogeneities such as large low-shear-velocity provinces (LLSVPs) (6, 7), and that of experimental iron spin-pairing in mantle minerals at lower-mantle depths (8, 9), has fueled a number of investigations of iron partitioning in the lower mantle (10–22).

Despite remarkable advances in experimental and analytical techniques in the last two decades (*Supporting Information*), stark discrepancies have been reported, depending on the composition of the starting material (San Carlos olivine vs. pyrolite) and differences in iron valence (Fe^{2+} and Fe^{3+}). San Carlos olivine has a molar (Mg + Fe)/Si = 2 and contains only iron as Fe^{2+}, whereas pyrolite has a molar (Mg + Fe)/Si = 1.4, contains Ca and Al, and contains iron as Fe^{2+} and Fe^{3+} (23). Therefore, the parameters controlling iron partitioning in deep mantle conditions are complex (12), and hinder any attempts to infer large-scale geophysical or geochemical consequences on the mantle.

To disentangle valence (15, 23), spin (18, 24), and compositional (12) effects on iron partitioning, we measured iron concentration and iron valence (Fe^{2+} and Fe^{3+} concentrations) in silicates and Fp at lower-mantle conditions, in two bulk compositions intermediate between the widely studied San Carlos olivine (10, 11, 17–19, 24, 25) and pyrolite (16, 21, 22) compositions. These are (*i*) an alumina-bearing olivine and (*ii*) a calcium-free pyrolite. Neither composition exists in nature, and they were therefore synthesized in the laboratory to be used as compositionally intermediate compounds: Al-bearing olivine is a San Carlos olivine (Mg#90) with the addition of 2 wt.% Al_2O_3, and has an iron valence distribution similar to that of pyrolite. Ca-free pyrolite has the same iron valence as pyrolite, but contains no Ca, eliminating CaPv from the phase assemblage; as CaPv contains negligible Fe, it is not relevant to Fe partitioning at lower-mantle conditions.

Materials and Methods

Al-bearing olivine and Ca-free pyrolite glasses were produced in an aerodynamic levitation laser furnace, compressed in symmetrical diamond anvil cells at pressures between 28 GPa and 118 GPa, and laser-heated from both sides to temperatures between 2,100 K and 2,700 K, sticking as close as possible to a mantle geotherm (26) (Table S1). The samples were heated for 10 min to 20 min to ensure full equilibration of the sample and to grow large enough crystal grains for accurate chemical quantification (Fig. 1*A* and *Supporting Information*). The samples were then quenched and decompressed, and thin sections suitable for transmission electron microscopy (TEM) analysis were prepared using the focused ion beam (FIB) lift-out technique (Fig. S1) using Zeiss Nvision 40 [Centre Interdisciplinaire de Microscopie Électronique (CIME), École Polytechnique Fédérale de Lausanne (EPFL)] and Zeiss Auriga [Institut de Physique du Globe de Paris (IPGP)] instruments. Quantitative chemical maps and analyses were obtained in scanning TEM (STEM) mode (Fig. 1 *B–D* and *Supporting Information*) using energy dispersive X-ray (EDX) spectroscopy (Fig. S2) performed on an FEI Tecnai Osiris TEM (CIME, EPFL). Iron valence state (Fe^{2+} and Fe^{3+} distribution) (Fig. S3) was measured on aberration-corrected electron microscopes, with high spatial resolution and high analytical sensitivity, by electron energy loss spectroscopy (EELS) on a JEOL ARM 200 instrument [LeRoy Eyring Center for Solid

Significance

We studied high-pressure and high-temperature phase equilibria using state-of-the-art microanalytical techniques to measure iron partitioning and valence in iron-bearing lower-mantle rocks. Our data allow us to reconcile the discrepancies observed in previous reports, and to propose a comprehensive model of the evolution of iron partitioning in the lower mantle. We reveal an intricate interplay between spin and valence states. Our results suggest a mineral physics basis for rheological variations in the deep lower mantle as a process for stabilizing large thermochemical piles and large low-shear-velocity provinces.

Author contributions: J.B. and P.G. designed research; H.P. and J.B. performed research; H.P., J.B., F.N., T.D., S.-H.S., M.C., and C.H. contributed new reagents/analytic tools; H.P., J.B., F.N., T.D., S.-H.S., and M.C. analyzed data; and H.P. and J.B. wrote the paper.

The authors declare no conflict of interest.

This article is a PNAS Direct Submission.

[1]To whom correspondence should be addressed. Email: helene.piet@epfl.ch.

This article contains supporting information online at www.pnas.org/lookup/suppl/doi:10.1073/pnas.1605290113/-/DCSupplemental.

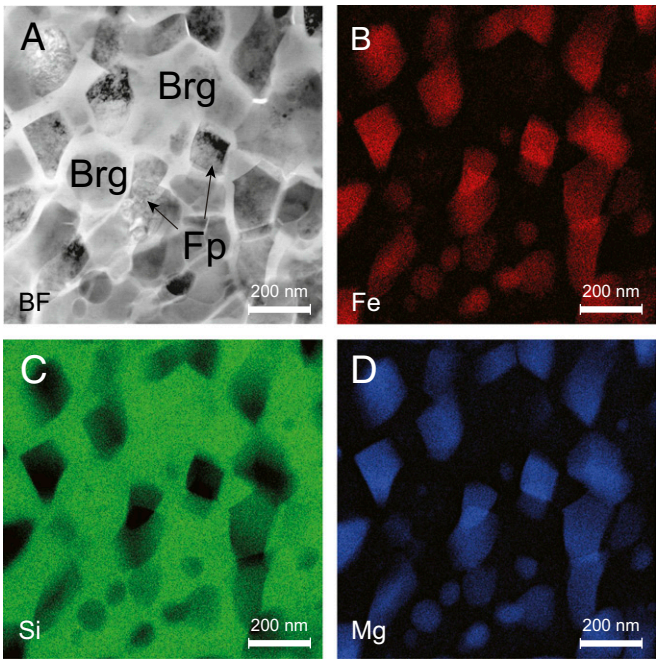

Fig. 1. TEM image and EDX chemical maps of a Brg and Fp assemblage heated for 15 min at 58 GPa and 2,400 K. Bright-field TEM image (*A*) of the assemblage and corresponding chemical maps for (*B*) iron, (*C*) silicon, and (*D*) magnesium. The geometry of Fp grains, as well as the identical composition of distinct grains across the sample, is indicative of equilibrium conditions. The central part of the sample shows smaller overlapping Fp and Brg grains; those were never used for quantification.

State Science, Arizona State University (ASU)] using a Gatan Enfinium spectrometer, and on an FEI Titan Themis instrument (CIME, EPFL) using a Gatan GIF Quantum ERS high energy-resolution spectrometer. Quantitative chemical analyses of silicates and Fp phases are reported in Table S1 for all runs, and more details about sample preparation, synthesis, recovery, and analysis can be found in *Supporting Information*.

Results and Discussion

The EELS measurements confirm that Fp, like olivine at lower-pressure conditions, does not accommodate ferric iron (Table S1), and contains only Fe^{2+} up to 118 GPa, as observed at lower pressures (15). The silicate, however, contains both Fe^{2+} and Fe^{3+}, consistent with previous observations (23, 27), albeit with significantly lower $Fe^{3+}/\Sigma Fe$ above 116 GPa (PPv stability field) than at lower pressure (Brg stability field). Ferric iron is therefore entirely contained in the silicate phase and doesn't exchange or partition between the silicate and Fp, whereas ferrous iron is distributed between both silicate and Fp through an Fe–Mg exchange reaction,

$$\left(Fe^{2+}\right)_{Sil} + \left(Mg^{2+}\right)_{Fp} \leftrightarrow \left(Mg^{2+}\right)_{Sil} + \left(Fe^{2+}\right)_{Fp}.$$

This reaction describes Fe^{2+} partitioning between both phases, and its exchange constant K_D is defined as $K_D = (X^{Sil}_{Fe^{2+}} \; X^{Fp}_{Mg^{2+}})/(X^{Fp}_{Fe^{2+}} \; X^{Sil}_{Mg^{2+}})$, where X is the (molar) concentration of Mg and Fe^{2+} in Fp and the silicate. The effective equilibrium constant K_{eff} describes total iron ($Fe^{2+} + Fe^{3+}$) partitioning between the two phases, $K_{eff} = (X^{Sil}_{Fe} \; X^{Fp}_{Mg})/(X^{Fp}_{Fe} \; X^{Sil}_{Mg})$, where X is now the (molar) concentration of Mg and total Fe in Fp and the silicate. High values of K_{eff} therefore indicate iron-rich silicates, whereas low values indicate iron-rich Fp.

The compositional effect on K_{eff} is apparent in Fig. 2*A*, where our data are combined with laser-heated diamond anvil cell (LHDAC) data from the literature obtained with other bulk chemistries (i.e., San Carlos olivine in blue, and pyrolite in orange). Our measurements in both Al-bearing olivine and Ca-free pyrolite are fully consistent with the previously published pyrolite dataset (16, 21, 22), corroborating the fact that iron partitioning is mainly controlled by aluminum content, and does not depend on the relative iron, magnesium, silicon, or calcium concentrations in the rock. Below 70 GPa, where partitioning is constant with pressure, K_{eff} in the Al-bearing system is significantly larger than in the Al-free system; this relative enrichment of iron in the Brg is the result of the coupled substitution $Fe^{2+} + Si^{4+} = Fe^{3+} + Al^{3+}$ (Fig. S4), stabilizing Fe^{3+} in that phase (28, 29).

The pressure effects on K_{eff} are more complex. At pressures up to 70 GPa, K_{eff} is effectively constant (Fig. 2*A*) in both types (Al-free and Al-bearing) of systems. The invariance of K_{eff} demonstrates that iron partitioning between lower-mantle minerals is constant with depth down to about 1,700 km depth, regardless of Al content and iron valence distribution, and is consistent with the absence of strong geophysical signature in the lower mantle to those depths (6, 30); 70 GPa corresponds to the onset of iron spin-pairing in Fp (8, 31), where iron enrichment was predicted (32, 33) in this phase. This enrichment is observed in both systems (Fig. 2*A*) through the decrease of K_{eff} above 70 GPa, with a notable difference, however: The Al-free system shows a gradual and constant decrease in K_{eff} (in this case equal to K_D) with pressure up to 100 GPa, whereas the Al-bearing system shows a peculiar behavior, in which K_{eff} decreases to a minimum value at 85 GPa and then increases up to 110 GPa.

In the PPv (3, 4) stability field, a sharp decrease in K_{eff} is observed in the Al-bearing system whereas a sharp increase is observed in the Al-free system. It is noteworthy, however, that K_{eff} then becomes identical (within uncertainties) in both Al-free and Al-bearing systems. This particularity is preserved at higher pressures in the PPv stability field, and both systems exhibit similar partitioning with K_{eff} decreasing with pressure; this is the only pressure range, corresponding to the lowermost mantle, where iron partitioning in both Al-free and Al-bearing systems is identical.

The comprehensive dataset clearly distinguishes two types of behavior: Al-free ferrous-iron-bearing systems (San Carlos olivine starting compositions, blue colors in Fig. 2*A*) and Al-bearing systems, containing both ferrous and ferric species (pyrolite, Ca-free pyrolite, and Al-bearing olivine, orange colors in Fig. 2*A*). This resolves the long-standing discrepancy in iron partitioning behavior previously reported in the literature, as being due to the inappropriate comparison of experimental data from Al-bearing and Al-free lithologies. Our data also confirm that iron partitioning in the Al-bearing system is more complicated than that in the Al-free system. The mechanism is explained by changes in iron valence in the silicate at high pressure coupled with changes in spin state. Iron depletion in the silicate (Brg or PPv) is systematically associated with a drop in Fe^{3+} concentration (Fig. 2*B*), and conversely; the evolution trends of K_{eff} (Fig. 2*A*) and Fe^{3+} concentration in the silicate (Fig. 2*B*) are identical. A drop in Fe^{3+} implies an increase in Fe^{2+} concentration, and the latter has a strong affinity for Fp as shown by the partitioning behavior in the Al-free system, especially above 70 GPa when it turns to the low-spin state. Therefore, iron depletion from the silicate is expected with decreasing Fe^{3+} and increasing Fe^{2+} concentration, due to the preferential partitioning of Fe^{2+} in Fp; that partitioning is spin-state-dependent, and becomes more extreme at pressures above 70 GPa, where iron becomes low-spin in Fp.

The combined dataset presented here also shows that iron partitioning in all Al-bearing systems (pyrolite, Ca-free pyrolite, Al-bearing olivine) is identical within uncertainties, regardless of bulk composition, and argues that our results are applicable to Earth's mantle. With the silicate phase being the dominant interconnected phase in the lower mantle, it should strongly

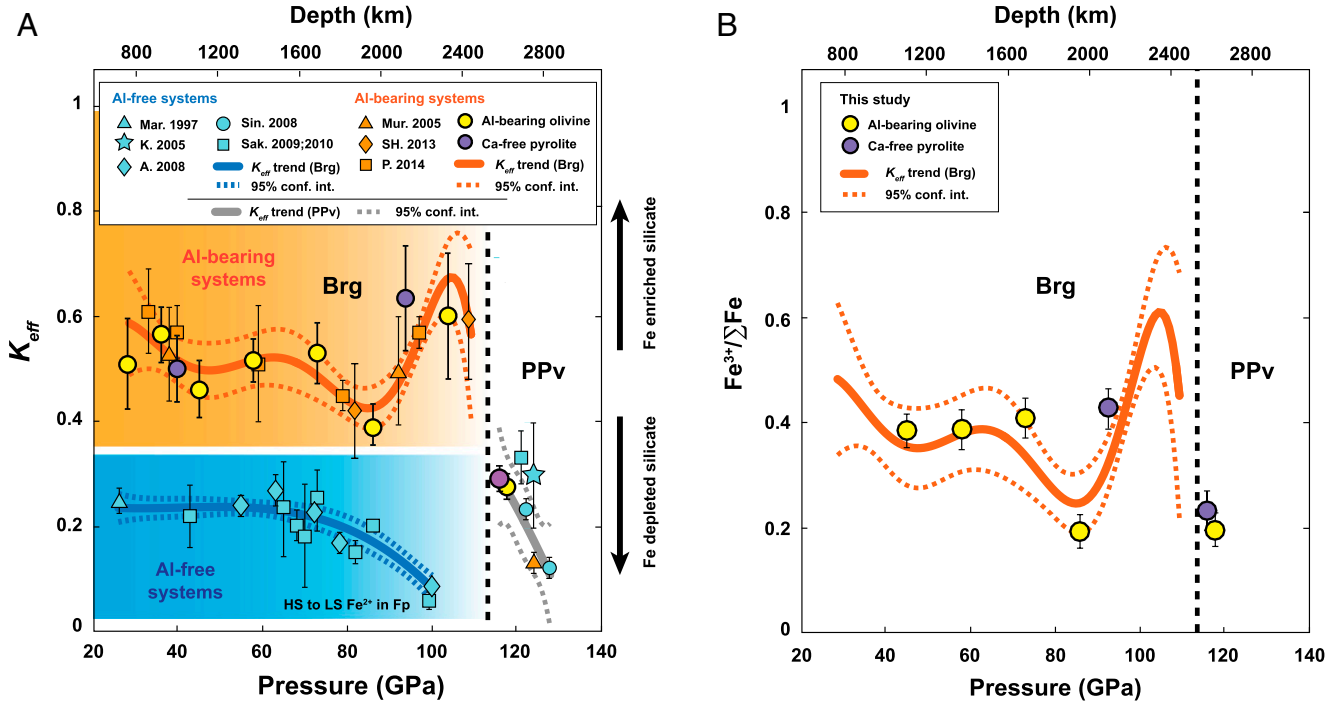

Fig. 2. Fe–Mg exchange coefficient between silicate (BRG and PPV) and Fp at lower-mantle pressures and temperatures. Brg and PPv stability fields are separated by the vertical dashed line at ~115 GPa. (*A*) Effective exchange coefficients K_{eff} obtained from EDX analyses (yellow and purple filled circles) are plotted as a function of pressure. K_{eff} values from previous studies in the San Carlos olivine system (11, 17–19, 24, 25) and in the pyrolite system (16, 21, 22) are also plotted (see *Supporting Information* for details). The blue-shaded area delimits the K_{eff} range for Al-free systems, and the orange-shaded are delimits that of Al-bearing systems. Solid lines running through the data were obtained by linear least-squares regression, and the 95% confidence intervals were calculated from the linear model by propagating experimental uncertainties (see *Supporting Information*); these mostly serve the purpose of showing that K_{eff} variations above 70 GPa are statistically resolvable. (*B*) Fe^{3+} concentration in the silicate as a function of pressure from EELS measurements. The line is not fit to the data but is replicated from that obtained in *A*. The notable match is a strong indication that iron partitioning between lower-mantle minerals in an Al-bearing system follows the evolution of iron valence (i.e., Fe^{2+} and Fe^{3+}) distribution in the silicate.

influence transport properties (34–36) and, most notably, viscosity (37). Although there are no compositional-dependence deformation data on Brg, experiments on olivine (38) and Fp (39) have shown an inverse correlation between iron content and strength: Minerals with higher iron concentrations are softer. Assuming that the strength of Brg/PPv follows a similar compositional dependence, an increase in K_{eff} should result in decreased strength. Because Brg/PPv is the major interconnected phase in the lower mantle, this should result in lowering mantle viscosities (9).

We found a striking correlation (Fig. S5) between mantle viscosity profiles obtained by geophysical inversion (40) and iron partitioning (K_{eff}); a viscosity maximum observed at 2,000 km depth corresponds to a minimum in both K_{eff} and $Fe^{3+}/\Sigma Fe$ observed at 85 GPa (Fig. 2), whereas the viscosity minimum at 2,550 km depth fits with a maximum in both K_{eff} and $Fe^{3+}/\Sigma Fe$ at 100 GPa (Fig. 2). The lack of sensitivity at those depths, however, precludes the accurate inference of viscosity from geophysical data (41, 42). Moreover, without composition-dependent deformation experiments or calculations on Brg, the question remains open from the point of view of mineral physics.

It has been proposed that the viscosity high at 1,000 km (40, 42, 43) is correlated with stagnating slabs and fast regions inferred from seismic tomography (44). If the viscosity contrast between 80 GPa and 120 GPa predicted here were to affect mantle dynamics below 1,800 km, this would provide a unique explanation to the remnance of LLSVPs. These structures are currently thought of as being primordial (7), dating back to the initial settling and freezing of Earth's Magma Ocean after accretion 4.5 Gy ago. The question of their stability (45), and how they anchor above the core–mantle boundary over geologic time, is still unsolved. The top of the weak layer inferred by our partitioning data sits above those structures. We propose that a weak lowermost mantle (below 2,000 km) topped by a stiffer mantle (1,800 km to 2,000 km) could dynamically decouple the base of the mantle from the overlying mantle, which could, in turn, isolate and stabilize these large structures.

ACKNOWLEDGMENTS. J. Mardinly and A. Toshi assisted with the ACEM measurements at ASU. We thank Richard Gaál, Fabienne Bobard, Susannah Dorfman (EPFL), and Stefan Borensztajn (IPGP) for experimental assistance. We thank Frederick Ryerson for fruitful discussions and meticulous enhancement of the manuscript. We thank two anonymous reviewers, whose comments allowed us to significantly improve the manuscript. S.-H.S. thanks NASA's Nexus for Exoplanet System Science (NExSS) research coordination network, sponsored by NASA's Science Mission Directorate, for partial support on the EELS measurements. The research received funding from the Swiss National Science Foundation through FNS Grant 200021_140474. This work was supported by the European Research Council (ERC) under the European Community's Seventh Framework Programme (FP7/2007-2013)/ERC Grant Agreement 207467, the UnivEarthS Labex program at Sorbonne Paris Cité (ANR-10-LABX-0023 and ANR-11-IDEX-0005-02), IPGP multidisciplinary program PARI, and Region Île-de-France SESAME Grant 12015908. S.-H.S. is supported by the National Science Foundation (EAR-1301813).

1. Murakami M, Hirose K, Kawamura K, Sata N, Ohishi Y (2004) Post-perovskite phase transition in $MgSiO_3$. *Science* 304(5672):855–858.
2. Hirose K, Sinmyo R, Sata N, Ohishi Y (2006) Determination of post-perovskite phase transition boundary in $MgSiO_3$ using Au and MgO pressure standards. *Geophys Res Lett* 33(1):L01310.
3. Catalli K, Shim S-H, Prakapenka V (2009) Thickness and Clapeyron slope of the post-perovskite boundary. *Nature* 462(7274):782–785.
4. Grocholski B, Catalli K, Shim S-H, Prakapenka V (2012) Mineralogical effects on the detectability of the postperovskite boundary. *Proc Natl Acad Sci USA* 109(7):2275–2279.

5. Hirose K, Takafuji N, Fujino K, Shieh SR, Duffy TS (2008) Iron partitioning between perovskite and post-perovskite: A transmission electron microscope study. *Am Mineral* 93(10):1678–1681.
6. Garnero EJ, Mcnamara AK (2008) Structure and dynamics of Earth's lower mantle. *Science* 320(5876):626–628.
7. Dziewonski AM, Lekic V, Romanowicz BA (2010) Mantle anchor structure: An argument for bottom up tectonics. *Earth Planet Sci Lett* 299(1-2):69–79.
8. Badro J, et al. (2003) Iron partitioning in Earth's mantle: Toward a deep lower mantle discontinuity. *Science* 300(5620):789–791.
9. Badro J, et al. (2004) Electronic transitions in perovskite: Possible nonconvecting layers in the lower mantle. *Science* 305(5682):383–386.
10. Guyot F, Madon M, Peyronneau J, Poirier JP (1988) X-ray microanalysis of high-pressure/high-temperature phases synthesized from natural olivine in a diamond-anvil cell. *Earth Planet Sci Lett* 90(1):52–64.
11. Martinez I, Wang Y, Guyot F (1997) Microstructures and iron partitioning in (Mg, Fe) SiO_3 perovskite-(Mg, Fe) O magnesiowüstite assemblages: An analytical transmission electron microscopy study. *J Geophys Res* 102(B3):5265–5280.
12. Mao H, Shen G, Hemley RJ (1997) Multivariable dependence of Fe-Mg partitioning in the lower mantle. *Science* 278(5346):2098–2100.
13. Andrault D (2001) Evaluation of (Mg,Fe) partitioning between silicate perovskite and magnesiowustite up to 120 GPa and 2300 K. *J Geophys Res* 106(B2):2079–2087.
14. Kesson S, Fitz Gerald J, O'Neill HS, Shelley JM (2002) Partitioning of iron between magnesian silicate perovskite and magnesiowüstite at about 1 Mbar. *Phys Earth Planet Inter* 131(3-4):295–310.
15. Frost DJ, Langenhorst F (2002) The effect of Al_2O_3 on Fe–Mg partitioning between magnesiowüstite and magnesium silicate perovskite. *Earth Planet Sci Lett* 199(1-2): 227–241.
16. Murakami M, Hirose K, Sata N, Ohishi Y (2005) Post-perovskite phase transition and mineral chemistry in the pyrolitic lowermost mantle. *Geophys Res Lett* 32(3):1–4.
17. Kobayashi Y, et al. (2005) Fe-Mg partitioning between (Mg, Fe)SiO_3 post-perovskite, perovskite, and magnesiowüstite in the Earth's lower mantle. *Geophys Res Lett* 32(19):L19301.
18. Auzende AL, et al. (2008) Element partitioning between magnesium silicate perovskite and ferropericlase: New insights into bulk lower-mantle geochemistry. *Earth Planet Sci Lett* 269(1-2):164–174.
19. Sinmyo R, et al. (2008) Partitioning of iron between perovskite/postperovskite and ferropericlase in the lower mantle. *J Geophys Res Solid Earth* 113(B11):B11204.
20. Irifune T, et al. (2010) Iron partitioning and density changes of pyrolite in Earth's lower mantle. *Science* 327(5962):193–195.
21. Sinmyo R, Hirose K (2013) Iron partitioning in pyrolitic lower mantle. *Phys Chem Miner* 40(2):107–113.
22. Prescher C, Langenhorst F, Dubrovinsky LS, Prakapenka VB, Miyajima N (2014) The effect of Fe spin crossovers on its partitioning behavior and oxidation state in a pyrolitic Earth's lower mantle system. *Earth Planet Sci Lett* 399:86–91.
23. McCammon C (1997) Perovskite as a possible sink for ferric iron in the lower mantle. *Nature* 387(6634):694–696.
24. Sakai T, et al. (2009) Fe-Mg partitioning between perovskite and ferropericlase in the lower mantle. *Am Mineral* 94(7):921–925.
25. Sakai T, et al. (2010) Fe–Mg partitioning between post-perovskite and ferropericlase in the lowermost mantle. *Phys Chem Miner* 37(7):487–496.
26. Shankland TJ, Brown JM (1985) Homogeneity and temperatures in the lower mantle. *Phys Earth Planet Inter* 38(1):51–58.
27. Sinmyo R, Hirose K, O'Neill HSC, Okunishi E (2006) Ferric iron in Al-bearing post-perovskite. *Geophys Res Lett* 33(12):12–14.
28. Richmond NC, Brodholt JP (1998) Calculated role of aluminium in the incorporation of ferric iron into magnesium silicate perovskite. *Am Mineral* 83(1985):947–951.
29. Brodholt JP (2000) Pressure-induced changes in the compression mechanism of aluminous perovskite in the Earth's mantle. *Nature* 407(6804):620–622.
30. Tackley PJ (2012) Dynamics and evolution of the deep mantle resulting from thermal, chemical, phase and melting effects. *Earth Sci Rev* 110(1-4):1–25.
31. Lin J-F, et al. (2005) Spin transition of iron in magnesiowüstite in the Earth's lower mantle. *Nature* 436(7049):377–380.
32. Lin JF, Speziale S, Mao Z, Marquardt H (2013) Effects of the electronic spin transitions of iron in lower mantle minerals: Implications for deep mantle geophysics and geochemistry. *Rev Geophys* 51(2012):244–275.
33. Badro J (2014) Spin transitions in mantle minerals. *Annu Rev Earth Planet Sci* 42(1): 231–248.
34. Xu Y, McCammon C, Poe BT (1998) The effect of alumina on the electrical conductivity of silicate perovskite. *Science* 282(5390):922–924.
35. Goncharov AF, Beck P, Struzhkin VV, Haugen BD, Jacobsen SD (2009) Thermal conductivity of lower-mantle minerals. *Phys Earth Planet Inter* 174(1-4):24–32.
36. Ammann MW, Brodholt JP, Wookey J, Dobson DP (2010) First-principles constraints on diffusion in lower-mantle minerals and a weak D'' layer. *Nature* 465(7297): 462–465.
37. Girard J, Amulele G, Farla R, Mohiuddin A, Karato S (2016) Shear deformation of bridgmanite and magnesiowüstite aggregates at lower mantle conditions. *Science* 351(6269):144–147.
38. Zhao YH, Zimmerman ME, Kohlstedt DL (2009) Effect of iron content on the creep behavior of olivine: 1. Anhydrous conditions. *Earth Planet Sci Lett* 287(1-2):229–240.
39. Tommaseo CE, Devine J, Merkel S, Speziale S, Wenk HR (2006) Texture development and elastic stresses in magnesiowustite at high pressure. *Phys Chem Miner* 33(2): 84–97.
40. Forte AM, Mitrovica JX (2001) Deep-mantle high-viscosity flow and thermochemical structure inferred from seismic and geodynamic data. *Nature* 410(6832):1049–1056.
41. Mitrovica JX, Forte M (2004) A new inference of mantle viscosity based upon joint inversion of convection and glacial isostatic adjustment data. *Earth Planet Sci Lett* 225(1-2):177–189.
42. Rudolph ML, Lekić V, Lithgow-Bertelloni C (2015) Viscosity jump in Earth's mid-mantle. *Science* 350(6266):1349–1352.
43. Justo JF, Morra G, Yuen DA (2015) Viscosity undulations in the lower mantle: The dynamical role of iron spin transition. *Earth Planet Sci Lett* 421:20–26.
44. Marquardt H, Miyagi L (2015) Slab stagnation in the shallow lower mantle linked to an increase in mantle viscosity. *Nat Geosci* 8(4):311–314.
45. Huang C, Leng W, Wu Z (2015) Iron-spin transition controls structure and stability of LLSVPs in the lower mantle. *Earth Planet Sci Lett* 423:173–181.
46. Hennet L, et al. (2006) Levitation apparatus for neutron diffraction investigations on high temperature liquids. *Rev Sci Instrum* 77(5):053903.
47. Akahama Y, Kawamura H (2006) Pressure calibration of diamond anvil Raman gauge to 310 GPa. *J Appl Phys* 100(4):043516.
48. Benedetti LR, Loubeyre P (2004) Temperature gradients, wavelength-dependent emissivity, and accuracy of high and very-high temperatures measured in the laser-heated diamond cell. *High Press Res* 24(4):423–445.
49. van Aken PA, Liebscher B (2002) Quantification of ferrous/ferric ratios in minerals: New evaluation schemes of Fe L 23 electron energy-loss near-edge spectra. *Phys Chem Miner* 29(3):188–200.
50. Sinmyo R, Hirose K, Muto S, Ohishi Y, Yasuhara A (2011) The valence state and partitioning of iron in the Earth's lowermost mantle. *J Geophys Res Solid Earth* 116(B7): B07205.

Supporting Information

Piet et al. 10.1073/pnas.1605290113

SI Materials and Methods

Starting Material Preparation. High-purity powders of MgO, FeO, and SiO_2 were finely ground and mixed together under ethanol to produce a natural San Carlos olivine composition (9.6 wt.% FeO). High-purity alumina powder was added to the mix to obtain a total Al_2O_3 concentration of 2.0 wt.% (Table S1). The powders were dried and pressed into pellets, and then fused at 2,100 °C for 60 s in an aerodynamic levitation laser furnace (46) using argon carrier gas. Temperature was quenched at 1,000 K/s to obtain a glass. A chip from each sample was then imaged with back-scattered electrons using a field-emission scanning electron microscope. The sample was homogeneous and contained no grains at any scale; further EDX analyses of the starting material were performed, and they revealed no chemical heterogeneities in the sample for all elements.

High-Pressure and High-Temperature Synthesis. Chips of the glassy starting material were pressurized in symmetrical diamond anvil cells, in a laser-drilled rhenium gasket (30 μm to 45 μm thick, 70- to 150-μm diameter hole). Flat 300-μm, 200-μm, and beveled 300/150-μm diamond culets were used. Pressure was measured from the Raman shift of previously calibrated diamond anvils (47). The samples were then laser-heated from both sides using a 200-W infrared fiber laser, to temperatures between 2,100 K and 2,450 K, sticking as close as possible to a mantle geotherm (26) (Table S1). Temperatures were measured by spectroradiometry (48). The samples were heated for 10 min to 20 min to ensure full equilibration of the sample and to grow large enough crystal grains for accurate chemical quantification. After laser heating, the samples were instantly quenched by switching off laser power. The samples were then decompressed and prepared for subsequent microanalysis.

Temperature gradients in the LHDAC can induce chemical (Soret) diffusion, which, in our case, is most critical for the case of iron toward the edges of the heated zone (i.e., outside the analyzed zone in the heated sample). However, we observe no significant variations in iron content of minerals analyzed in different parts of the heated zone, which precludes significant temperature gradients during the synthesis. We also report an average of less than 10% loss of iron in the center of the sample compared with the initial iron content in the starting material. Such iron losses are quite fair according to previous studies, where 40% could be lost toward the edges of the heated spot. More importantly, for each sample, K_{eff} was measured across the heated spot and showed no variation. Partitioning can be highly temperature-dependent, and what those measurements show is either that iron partitioning has a weak temperature dependence or that temperature variations across the parts of the sample where the measurements were performed are relatively limited.

Sample Preparation for TEM Analyses: The FIB Technique. Thin sections suitable for TEM analysis were prepared using the FIB lift-out technique (Fig. S1). We used Zeiss Nvision 40 (CIME, EPFL) and Zeiss Auriga (IPGP) instruments. We first deposited a 1.5-μm-thick carbon or platinum layer on top of the sample, in the zone corresponding to the center of the laser-heated area (Fig. S1 *A* and *B*). This layer prevents the sample from ion beam damage during excavation. The sample was excavated around the carbon deposit (Fig. S1*C*) using a focused gallium ion (Ga^+) beam operated at 30 kV and different currents in the 1- to 27-nA range. A (15 × 20 × 2)-μm section was then extracted with a micromanipulator and transferred to an omniprobe TEM copper grid for further thinning (Fig. S1*D*). We then switched to a lower range of currents (80 pA to 700 pA) for thinning the sample down to electron transparency. TEM analyses require a thickness of the sample between 50 nm and 100 nm. Given the uncertainty in thickness measurements while in ion imaging, we thinned the sample until we reached electron transparency in SEM imaging with the electron beam operated at 4 kV; this was enough to provide good quantitative analyses for the two quantitative techniques used and described hereafter (TEM-EDX and EELS). Final polishing of the thinned area was performed operating the ion beam voltage of 5 kV with a current of 30 pA to remove the deposition from the milling process.

Chemical Analyses by EDX Spectroscopy. Chemical analyses were obtained by EDX spectroscopy and performed using Analytical TEM on an FEI Tecnai Osiris (CIME, EPFL) operated at 200 kV to image the sample in Bright-Field (Fig. 1*A*) as well as High Angle Annular Dark Field modes. Typical EDX spectra are shown in Fig. S2. Chemical maps were acquired in STEM mode for 500 s to 1,000 s to minimize analytical uncertainties (Fig. 1 *B*–*D*). Quantitative measurements were then performed on individual grains by deconvolution of selected areas, after Bremsstrahlung background subtraction, using Fe, Mg, Si, O, and Al K alpha lines. A TEM thin section from the starting glass material was also prepared by FIB technique to provide the precise composition of the starting material, using the same quantification protocol as the high-pressure samples (Table S1).

Characterization of Iron Valence State by EELS. The ARM200 was operated in TEM mode at an accelerating voltage of 120 kV. To avoid electron beam-induced sample damage, particularly changes in the oxidation state of Fe, we expanded the electron beam (up to ∼200 nm in diameter, but smaller than the size of individual grains). With similar concerns regarding sample damage, the Titan showed optimal performance when operated at 300 kV using the dual-channel STEM-EELS acquisition for near-simultaneous low-loss and core-loss acquisition with a dispersion of 0.05 eV/channel. We chose a 2.5-mm entrance aperture for the spectrometer and a camera length of 29.5 mm, resulting in a collection angle of 19.8 mrad. On both microscopes, spectra were acquired for 10 s to 30 s, preventing beam damage of the silicate matrix and ensuring a good signal-to-noise ratio, enough for deconvolution of spectral features from acquired spectra.

The energy resolution was <1 eV, estimated from the full width at half maximum of the zero-loss peak. The fraction of ferric iron was determined by the EELS analysis methods in van Aken (49). In the analysis, we used the EEL spectra of olivine and pyroxene as a ferrous iron standard and the EEL spectrum of andradite as a ferric iron standard, all of which are measured using the instrument in the same analytical conditions as when measuring the samples. We subtracted the background following the method described in van Aken (49). A channel-to-channel gain variation and dark current correction were done for all EEL spectra. The spectra were then fitted by minimizing (least squares) the residual of the linear combination of ferrous and ferric iron standard spectra (Fig. S3).

SI Results and Discussion

TEM imaging and EDX mapping (Fig. 1) reveal that mineral assemblages are mainly composed of Fp grains embedded in an amorphous Brg matrix, in equal proportions as it is usually observed for samples equilibrated from olivine (18, 24). Fp grain size ranges between 50 nm and 400 nm, with a texture characteristic of

full chemical equilibration and growth (15, 18). We observe no significant chemical heterogeneities among minerals investigated in different areas of the samples. These observations preclude any substantial chemical diffusion (Soret) during laser heating that could have biased the chemical analyses. Fp grains used for quantification are essentially Si-free (Fig. 1*C*), ensuring no contamination from overlap with Brg in chemical analysis (Table S1).

Iron partitioning at lower-mantle conditions has been thoroughly investigated in the simple San Carlos olivine (10, 11, 17–19, 24, 25) and the complex pyrolite (16, 21, 22) systems. Besides the clear discrepancy in iron partitioning between these two systems (Fig. 2), discrepancies are also reported among data sets treating identical bulk compositions. In Fig. 2, we show only the experimental values of K_{eff} that were not affected by experimental artifacts, and are thus consistent with pressure (P) and temperature (T) conditions along the lower-mantle geotherm. We discuss the robustness of these data in *SI Results*, *Iron Partitioning Data* and refer to measured data as K_{eff} values. In the following sections, we discuss observed changes in Fe^{3+} content of the silicate with increasing pressure (*SI Results*, *Iron Valence State in BRG*) and the effect on mantle rheology (*SI Results*, *Viscosity in the Lower Mantle*).

Iron Partitioning Data from the Literature.

The San Carlos olivine system. Two studies (18, 24) report an increase of iron content in Fp from 70 GPa to 100 GPa, which they associate with the spin transition of ferrous iron from high-spin to low-spin state (8, 32). A volume collapse of iron following the spin transition indeed favors the incorporation of low-spin species into Mg sites, resulting in an increased affinity of iron for Fp (Fig. 2). However, other studies on iron partitioning in the San Carlos olivine system do not report this effect (17, 19).

Kobayashi et al. (17) report values of K_{eff} (below 0.2) in the Brg stability field systematically lower than all other studies; this could be due to the choice of low equilibration temperatures, several hundred Kelvin below the other studies (and far from a plausible mantle geotherm). For this reason, their data were discarded from our subsequent analysis. Sinmyo et al. (19) report strong heterogeneities in Fp compositions caused by extensive iron diffusion (Soret) toward the edges of the heated zone where temperatures are highest. Such nonequilibrium conditions preclude the use of such data for a proper thermodynamic quantification, as suggested by the authors. Hence, the data from that study were also discarded from subsequent analysis. Iron diffusion during laser heating is almost inevitable, but our samples only show minor iron depletion (less than 10% total iron loss).

Sakai et al. (25) report two significantly different values of K_{eff} measured in the same sample at 140 GPa. The sample experienced iron depletion in one part (K_{eff} = 0.44 ± 0.13) and iron enrichment in another part (K_{eff} = 0.04 ± 0.01), producing markedly different values due to accordingly different Fp compositions. Hence, that point was discarded from the dataset.

Auzende et al. (18) also measure an anomalously high K_{eff} value (0.66 ± 0.05) at 115 GPa compared with other data from the literature (K_{eff} below 0.5). They estimate the silicate to be PPv, despite the absence of XRD analysis. However, all subsequent measurements on the PPv phase showed markedly lower partitioning values. Hence, that anomalous point was discarded from the author's dataset.

The pyrolite system. The high value of K_{eff} (0.90 ± 0.14) at 114 GPa from Sinmyo and Hirose (21) is intriguing. In the study of Sinmyo et al. (50), that same sample was characterized as Brg, and pressure was estimated at 93 GPa (20 GPa lower), a difference which easily spans the Brg/PPv transition. Moreover, the K_{eff} value of ~1.12 in 2011 was recalculated at 0.90 in 2013. Such uncertainties on the conditions of synthesis preclude any use of that point in the global model. For the same reasons, the value of Sinmyo et al. (50) for PPv at 135 GPa (K_{eff} = 0.22) was also scrapped.

Prescher et al. (22) report a silicate phase as Brg although very clearly in the PPv stability field (130 GPa, 2,500 K), probably indicating metastable conditions during synthesis. The data point was also discarded. Our data above 110 GPa lack in situ characterization of the silicate structure (Brg vs. PPv). However, our measured K_{eff} values are identical to those observed by Sinmyo et al. (19), Sakai et al. (25), Kobayashi et al. (17), and Murakami et al. (16) where the silicate is confirmed as PPv by X-ray diffraction (XRD). Low ferric iron contents in PPv (25% ferric iron vs. 40% on average in Brg) are another argument supporting the PPv structure in our silicates at the highest pressures.

Iron Valence State in Brg. Charge neutrality of a crystallographic structure rules the possible cation substitutions in cation sites. In Brg, Fe^{2+}, for example, simply exchanges with Mg^{2+} in dodecahedral sites. On the other hand, the stabilization of Fe^{3+} in the structure is less straightforward, and aluminum is found to play a key role (15, 23). Among all possible substitution mechanisms investigated by Richmond and Brodholdt (28), the 1:1 coupled substitution of Fe^{3+} and Al^{3+}, respectively, in the dodecahedral Mg site and the octahedral Si site is the mechanism that requires the minimal amount of energy and hence the most favorable,

$$Fe^{2+}_{\text{A-site}} + Si^{4+}_{\text{B-site}} \rightarrow Fe^{3+}_{\text{A-site}} + Al^{3+}_{\text{B-site}}. \quad \textbf{[S1]}$$

A-site and B-site stands, respectively, for the dodecahedral Mg site and the octahedral Si site.

In Al-free systems or if Al content is too low to satisfy the conditions of Eq. **S1**, the incorporation of Fe^{3+} similarly involves the substitution of two Fe^{3+} in both the dodecahedral and the octahedral sites,

$$Fe^{2+}_{\text{A-site}} + Si^{4+}_{\text{B-site}} \rightarrow Fe^{3+}_{\text{A-site}} + Fe^{3+}_{\text{B-site}}, \quad \textbf{[S2]}$$

charge balancing the electronic structure of the mineral. In the case where Al^{3+} is in excess over Fe^{3+}, the incorporation of Al^{3+} follows the same mechanism,

$$Mg^{2+}_{\text{A-site}} + Si^{4+}_{\text{B-site}} \rightarrow Al^{3+}_{\text{A-site}} + Al^{3+}_{\text{B-site}}, \quad \textbf{[S3]}$$

entering adjacent dodecahedral and octahedral sites. These mechanisms do not involve the creation of oxygen vacancies.

At pressures below 75 GPa, Al/Fe^{3+} ratios in the silicate are close to unity, implying that ferric iron incorporation mainly occurs following the coupled substitution of the two species in Eq. **S1** (see also Fig. S4). However, above 75 GPa, Al/Fe^{3+} ratios significantly exceed 1, implying incorporation of excess aluminum through the mechanism described in Eq. **S3**.

Viscosity in the Lower Mantle. Experimental estimates of the viscosity of mantle minerals can be obtained by deformation experiments at high P and T. Such measurements on lower-mantle mineral assemblages have only been performed, to date, to pressures up to 28 GPa (37).

Fig. S5 shows that the trend of K_{eff} in the Brg stability field (Fig. 2*A*) is strongly anticorrelated with the radial viscosity profile determined by Forte and Mitrovica (40). This corroborates the idea that variations of the iron content in Brg are responsible for rheological variations observed in the mantle. Indeed, a decrease of iron content in Brg could make the material stronger, as is the case for olivine (38) and Fp (39), which might, in turn, affect the viscosity of the whole mantle. The rheological properties of a PPv-dominated mantle, on the other hand, would most likely be different from that of a Brg-dominated mantle, given the structural change and the different intrinsic viscosity of the mineral. However, the lack of sensitivity of the radial viscosity models at those depths does not allow estimation of any possible viscosity change associated with the phase transition in the silicate.

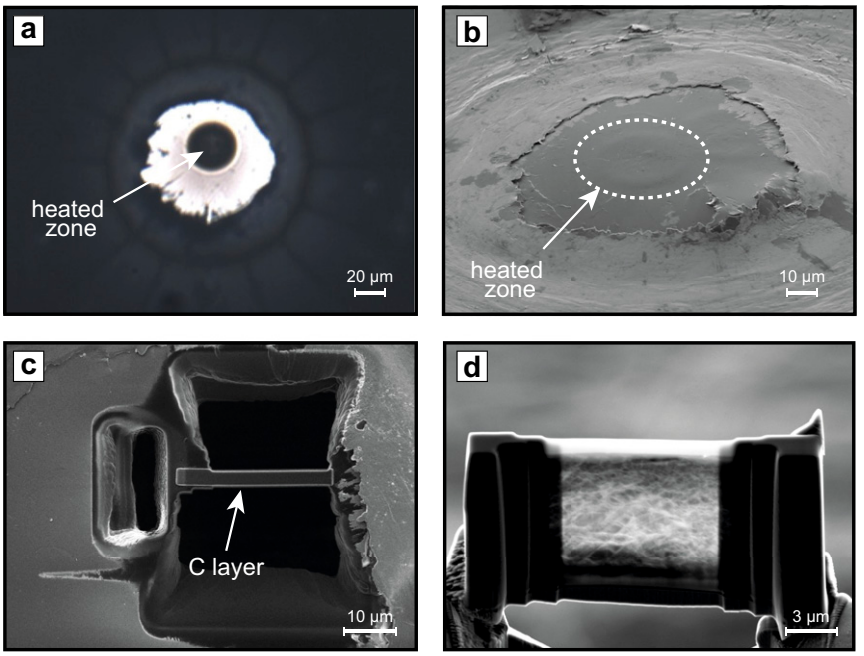

Fig. S1. Sample recovery by FIB technique. (*A*) Optical image of the sample viewed through the diamond anvils in situ at high pressure. The dark area represents the transformed and equilibrated (laser-heated) area. (*B*) Secondary electron image of the sample after decompression. (*C*) Gallium ion image of excavation, obtained after milling around the center of the heated spot, and protected on top by a carbon or a platinum layer. (*D*) Secondary electrons image of a transferred sample on a TEM Cu grid. The thin section is thinned to electron transparency (thickness < 100 nm) for EDX and EELS TEM analyses.

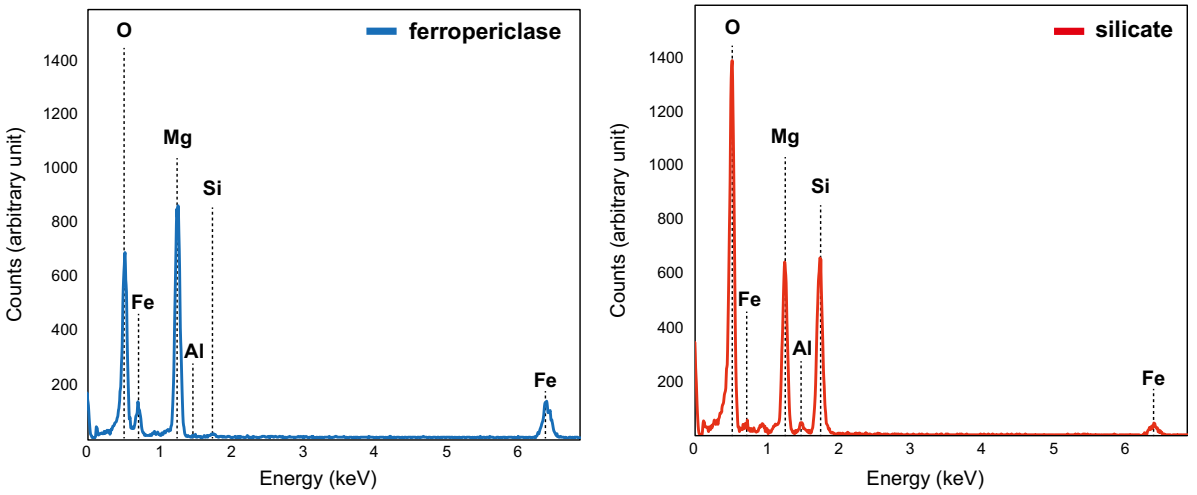

Fig. S2. EDX spectra for (*Left*) Fp and (*Right*) silicate. Energy distribution corresponds to X-ray emissions from characteristic chemical elements. Peak height is correlated to element concentration in the investigated zone. The spectrum for Fp shows no peak for Si and Al, in good agreement with the absence of these two elements in the mineral structure.

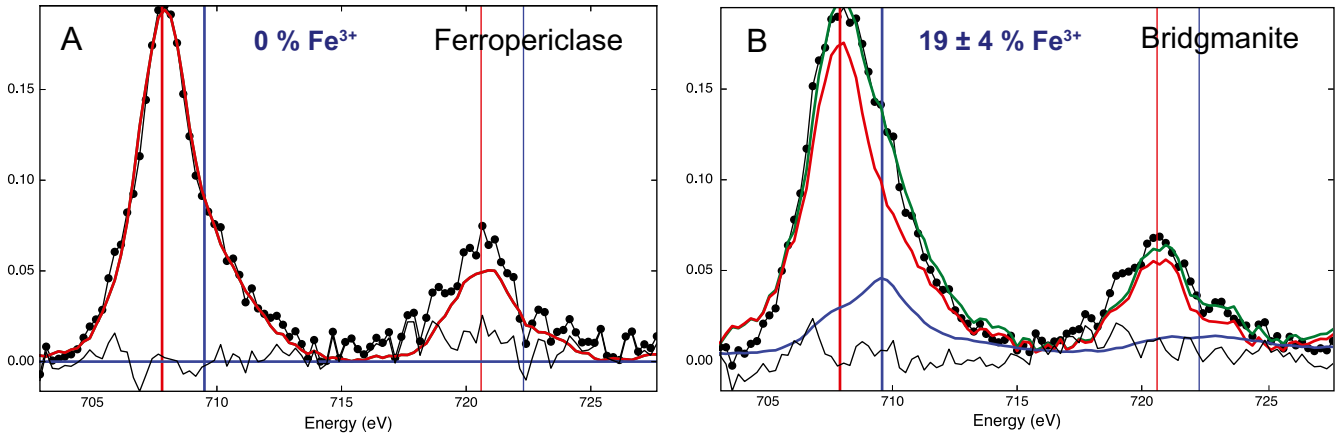

Fig. S3. EEL spectra of (*A*) Fp and (*B*) Brg. The black dots are measurements on the sample, whereas the red and blue curves are the measurements from the standards, olivine for pure Fe^{2+} and andradite for pure Fe^{3+}, respectively. The green curve is the calculated spectrum obtained by a least-squares fit using the two standards. The thin black line is the residual of the fit. The red and blue vertical bars mark the energies of the Fe^{3+} and Fe^{2+} peaks, respectively, showing a chemical shift of 1.5 eV. Fp shows no Fe^{3+} signature and is hence only composed of Fe^{2+} iron (*A*), whereas Brg (here at 86 GPa) has an $Fe^{3+}/\Sigma Fe$ value of 0.19 ± 0.03 (*B*).

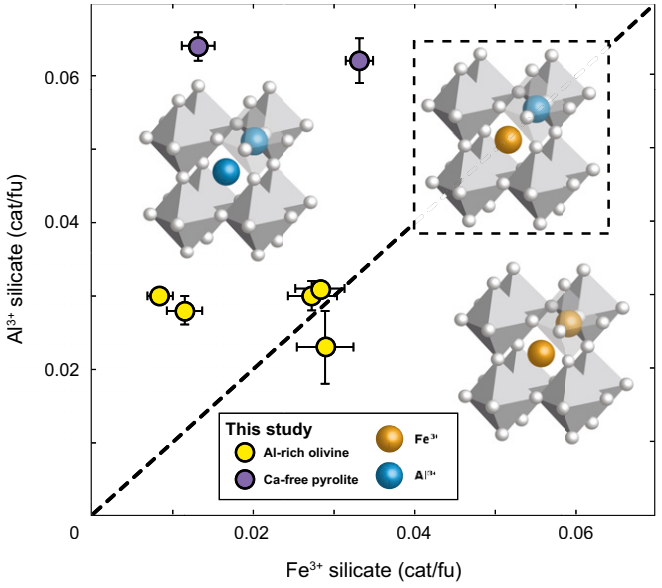

Fig. S4. Substitution mechanisms for incorporation of Fe^{3+} in the silicate structure. The most energetically favorable mechanism for stabilizing Fe^{3+} in the silicate structure is through the coupled substitution of Fe^{3+} in the dodecahedral site and Al^{3+} substitution in the octahedral site (Eq. **S1**). This reaction takes place along the black dashed line and requires equal amounts of Fe^{3+} and Al^{3+} in the silicate. When ferric iron (orange spheres) or aluminum (blue spheres) are in excess in the system, their incorporation in the silicate is possible via a similar mechanism (respectively, Eqs. **S2** and **S3**) where they charge-balance each other in adjacent sites.

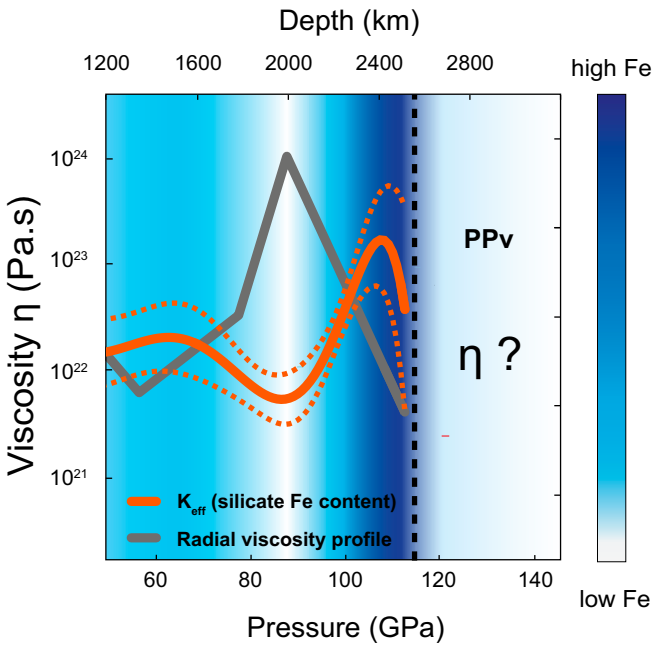

Fig. S5. Radial viscosity profile of Earth's lower mantle. Radial viscosity models proposed by Forte and Mitrovica (40) are plotted in gray. The orange curve is the superimposed iron partitioning (K_{eff}) evolution with pressure (from Fig. 1) for Al-bearing systems relevant to the lower mantle (the dashed part corresponds to 95% confidence interval). The blue–white color gradient is a visual representation of iron concentration in the silicate phase. The figure shows a striking correlation between increasing viscosity above 75 GPa and iron depletion in the silicate at the same pressure. Above 110 GPa, however, the silicate structure changes from Brg to PPv, where Fe concentration is even lower. However, the deformation mechanism as well as the very high anisotropy of the PPv phase preclude any simple assessment of the evolution of viscosity at this depth.

Table S1. Synthesis conditions of phase assemblages and corresponding chemical analyses

Run	SM-OL	SM-PYR	OL-28		OL-36		PYR-40		OL-45		OL-58		OL-73		OL-86		PYR-93		OL-104		PYR-116		OL-118	
P, GPa	oxides (wt.%)	oxides (wt.%)	28 (1)		36 (2)		40 (2)		45 (2)		58 (3)		73 (4)		86 (4)		93 (5)		104 (6)		116 (6)		118 (6)	
T, K			2,100 (100)		2,400 (200)		2,150 (125)		2,200 (100)		2,400 (50)		2,100 (50)		2,400 (100)		2,350 (150)		2,700 (200)		2,450 (130)		2,300 (75)	
Phase			sil	Fp	sil	Fp	sil	Fp	sil	Fp	sil	Fp	sil	Fp	sil	Fp	sil	Fp	sil	Fp	sil	Fp	sil	Fp
Mg	41.7 (11)	37.7 (12)	0.87 (7)	0.83 (9)	0.89 (2)	0.85 (8)	0.87 (2)	0.80 (3)	0.93 (3)	0.82 (15)	0.91 (2)	0.83 (11)	0.92 (3)	0.80 (18)	0.92 (2)	0.84 (6)	0.96 (3)	0.87 (20)	0.92 (1)	0.91 (11)	0.89 (2)	0.79 (13)	0.93 (2)	0.84 (6)
Fe*	9.9 (7)	8.2 (7)	0.077 (9)	0.14 (2)	0.074 (3)	0.13 (1)	0.091 (11)	0.17 (1)	0.071 (5)	0.14 (3)	0.073 (3)	0.13 (2)	0.071 (6)	0.12 (3)	0.060 (5)	0.14 (1)	0.077 (10)	0.11 (3)	0.04 (1)	0.07 (1)	0.057 (2)	0.18 (3)	0.043 (3)	0.14 (1)
Si	45.9 (6)	48.8 (6)	1.00 (5)	0.014 (5)	1.00 (2)	0.012 (2)	0.97 (2)	0.018 (1)	0.98 (2)	0.019 (8)	0.99 (3)	0.017 (7)	0.99 (2)	0.041 (12)	0.99 (3)	0.009 (3)	0.94 (4)	0.008 (5)	1.00 (2)	0.01 (1)	0.98 (2)	0.014 (9)	0.99 (1)	0.008 (3)
Al	2.5 (1)	5.2 (1)	0.038 (7)	0.002 (1)	0.031 (1)	0.002 (1)	0.062 (4)	0.002 (1)	0.030 (2)	0.003 (1)	0.031 (1)	0.001 (1)	0.023 (5)	0.001 (1)	0.028 (2)	0.001 (1)	0.062 (3)	0.002 (1)	0.02 (1)	0.01 (1)	0.064 (2)	0.003 (1)	0.030 (1)	0.001 (1)
K_{eff}			0.51 (9)		0.57 (5)		0.50 (6)		0.46 (6)		0.52 (4)		0.53 (6)		0.40 (4)		0.64 (11)		0.60 (12)		0.29 (2)		0.27 (3)	
$Fe^{3+}/\Sigma Fe$	0.25 (4)		—	—	—	—	—	—	0.38 (3)	ND	0.39 (4)	ND	0.41 (3)	ND	0.19 (3)	ND	0.43 (3)	ND	—	—	0.23 (4)	ND	0.20 (3)	ND

Temperature is determined from the average temperature over the entire run, and the value in parentheses corresponds to the maximum temperature variation during heating (this is not the 1-sigma SD). Pressure is measured from the first-order Raman peak of the anvils (47). Chemical composition of the starting material (SM) and of equilibrated samples of Fp and silicate (sil: Brg or PPv) are measured by TEM-EDX. Element concentrations for the silicate and Fp are given in cations per formula units; SDs are in parentheses. ND, not detected; OL, Al-rich olivine composition; PYR, Ca-free pyrolite composition.
*Fe is the total iron.